Research Article

Electrodeposition of Pt-Decorated $Ni(OH)_2$/CeO_2 Hybrid as Superior Bifunctional Electrocatalyst for Water Splitting

Huanhuan Liu, Zhenhua Yan [iD]**, Xiang Chen, Jinhan Li, Le Zhang, Fangming Liu, Guilan Fan, and Fangyi Cheng** [iD]

Key Laboratory of Advanced Energy Materials Chemistry (Ministry of Education), Renewable Energy Conversion and Storage Center, College of Chemistry, Nankai University, Tianjin 300071, China

Correspondence should be addressed to Zhenhua Yan; yzh@nankai.edu.cn and Fangyi Cheng; fycheng@nankai.edu.cn

The facile synthesis of highly active and stable bifunctional electrocatalysts to catalyze water splitting is attractive but challenging. Herein, we report the electrodeposition of Pt-decorated $Ni(OH)_2$/CeO_2 (PNC) hybrid as an efficient and robust bifunctional electrocatalyst. The graphite-supported PNC catalyst delivers superior hydrogen evolution reaction (HER) and oxygen evolution reaction (OER) activities over the benchmark Pt/C and RuO_2, respectively. For overall water electrolysis, the PNC hybrid only requires a cell voltage of 1.45 V at $10\,\mathrm{mA\,cm^{-2}}$ and sustains over 85 h at $1000\,\mathrm{mA\,cm^{-2}}$. The remarkable HER/OER performances are attributed to the superhydrophilicity and multiple effects of PNC, in which $Ni(OH)_2$ and CeO_2 accelerate HER on Pt due to promoted water dissociation and strong electronic interaction, while the electron-pulling Ce cations facilitate the generation of high-valence Ni OER-active species. These results suggest the promising application of PNC for H_2 production from water electrolysis.

Dedicated to the 100th anniversary of Chemistry at Nankai University

1. Introduction

Hydrogen is the ideal alternative of fossil fuels as an important clean energy and industrial material [1, 2]. Water electrolysis using electricity from renewable energy is a facile and attractive technique to produce hydrogen with high purity [3, 4]. Electrocatalysts play the paramount role in overcoming the slow dynamics of both hydrogen and oxygen evolution reactions (HER and OER) [5–7]. While Pt and Ru/Ir-based compounds are highly efficient to catalyze HER and OER, respectively [8, 9], their fancy price, extremely low elemental reserves, and unsatisfactory durability limit large-scale applications [10–12], calling for strategies to improve stability and reduce noble metal loading [13–15].

In alkaline media, although Pt is the benchmarking HER catalyst, its catalytic activity is still restrained by water dissociation due to the lack of oxyphilic surfaces to cleave the O −H bond of H_2O [16, 17]. The synergistic effect mechanism of Pt and $Ni(OH)_2$ has been indicated in previous studies: $Ni(OH)_2$ promotes the water dissociation and the generation

of hydrogen atoms, which are absorbed at Pt sites nearby to recombine into hydrogen molecules [18–24]. In addition, using a bifunctional catalyst could avoid different synthetic processes of electrocatalysts and simplify the water electrolysis device to lower the cost [25]. However, $Pt/Ni(OH)_2$ catalysts do not favor the OER due to sluggish kinetics. The electronic structure of Ni could be modulated through the integration of CeO_2 in $Ni(OH)_2$, which could further promote to form γ-NiOOH, making the $Ni(OH)_2$/CeO_2 a superb OER catalyst [26, 27]. Meanwhile, Ce can impose large electronic perturbation to Pt nanoparticles, which may enhance the HER ability of the neighboring Pt sites [28]. Therefore, the Pt-$Ni(OH)_2$-CeO_2 hybrid has great potential for electrocatalysis of both HER and OER but has not been reported previously. Besides, the Pt-based hybrid catalysts usually suffer from complicated preparation procedures, particle agglomeration, and weak adhesion between catalyst and substrate [29–31].

In this study, we report a facile electrodeposition method to synthesize ultrafine Pt nanoparticles (NPs) decorated
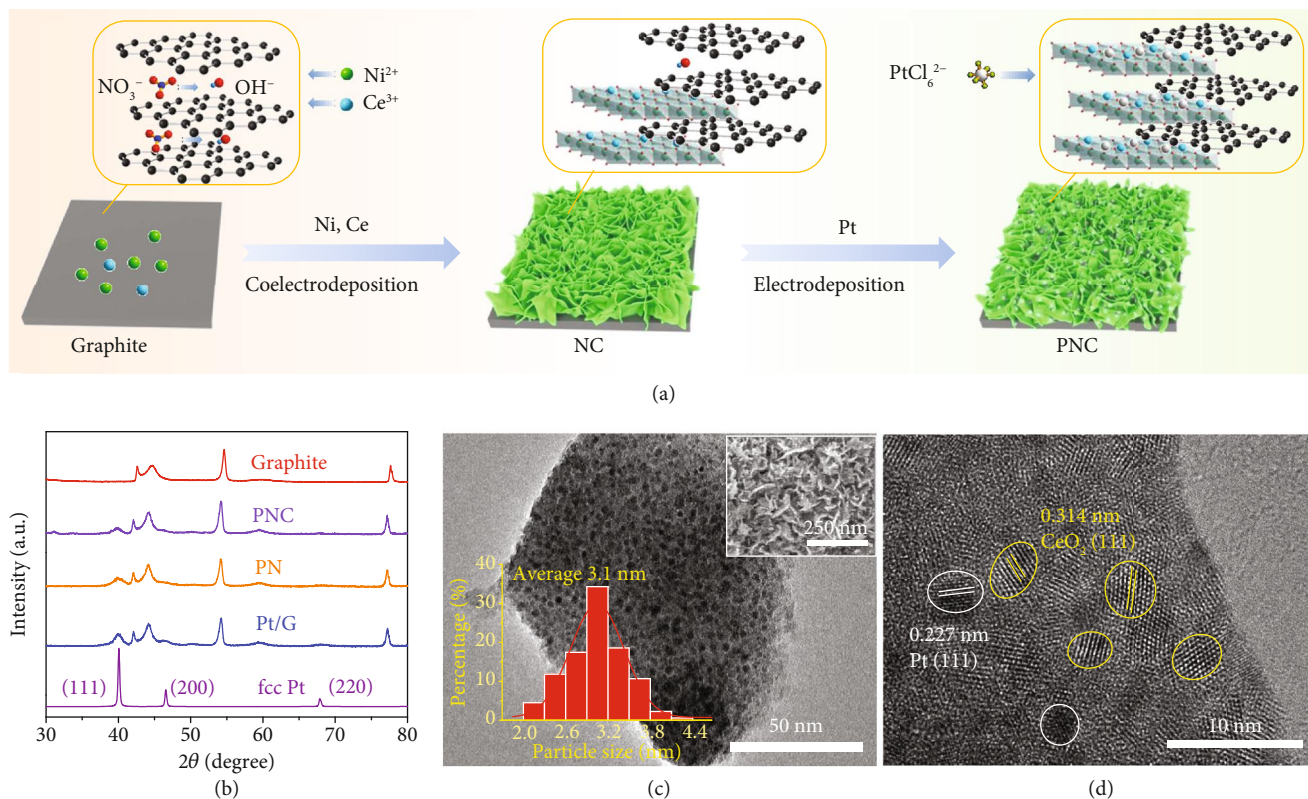
FIGURE 1: Synthesis and characterization of PNC. (a) Preparation diagram of PNC electrocatalyst on graphite. (b) XRD analysis of Pt/G, PN, and PNC. (c) TEM images of PNC. The inset shows the SEM image of PNC and the size distribution of Pt and CeO_2 NPs. (d) HRTEM images of PNC.

$Ni(OH)_2/CeO_2$ nanosheets (abbreviated as PNC) via anion intercalation and cathodic electrodeposition method. The Pt NPs with an average size of 3.1 nm are homogeneously deposited on the $Ni(OH)_2/CeO_2$ (abbreviated as NC) nanosheets, which could increase the exposure area of active sites and improve the utilization of Pt. Additionally, the mosaic-structured NC nanosheets not only effectively catalyze the OER but also enhance the HER activity of Pt due to electronic modulation and promoted dissociation of water. Furthermore, anion intercalation and in situ growth of the hybrid catalyst on graphite construct interfaces with strong adhesion, resulting in efficient electron transportation and enhanced stability. As a result, the prepared PNC electrocatalyst exhibits superior activity and stability to catalyze overall water electrolysis.

2. Result and Discussion

The PNC catalyst was synthesized through a two-step cathodic electrodeposition process as illustrated schematically in Figure 1(a). Graphite substrate was pretreated by applying a positive potential to allow nitrate ions inserting into graphite layers to enhance the interface of catalyst and graphite. The potential was reversed to realize the cathodic coelectrodeposition of cerium dioxide and nickel hydroxide on graphite. Subsequently, Pt NPs were deposited on the NC nanosheets to obtain the PNC hybrid electrode. In this two-step deposition process, the Pt loading can be reduced

and the exposure of Pt is increased to enhance the utilization of Pt, outperforming the reverse sequence when Pt is deposited prior to transition metal hydroxide. The involved reactions in the preparation of PNC are described by equations (1)–(4). For comparison, Pt/G and $Pt-Ni(OH)_2$ (abbreviated as PN) electrodes were obtained through a similar process.

$$NO_3^- + H_2O + 2e^- \longrightarrow 2OH^- + NO_2^- \qquad (1)$$

$$Ni^{2+} + 2OH^- \longrightarrow Ni(OH)_2\downarrow \qquad (2)$$

$$4Ce^{3+} + 12OH^- + O_2 \longrightarrow 4CeO_2\downarrow + 6H_2O \qquad (3)$$

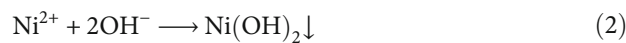$$PtCl_6^{2-} + 2H_2O \longrightarrow Pt\downarrow + 4H^+ + 6Cl^- + O_2\uparrow \qquad (4)$$

Figure 1(b) shows the X-ray diffraction (XRD) patterns of the prepared Pt, PN, and PNC. In addition to the reflections of graphite substrate, the diffraction peaks centered at 2θ of 40.0 and 46.5° correspond to the (111) and (200) planes of the face-centered cubic (fcc) Pt (space group of Fm-3m), respectively. The $Ni(OH)_2$ and CeO_2 signals are not observed in XRD because of weak crystalline state of $Ni(OH)_2$ and low content of CeO_2 (supplementary Figure S1). The morphology and microstructure were investigated by a scanning electron microscope (SEM) and transmission electron microscope (TEM). The prepared PN and PNC are composed of aggregated nanoparticles with interparticle pores and flat nanosheets with a thickness of 5–10 nm,
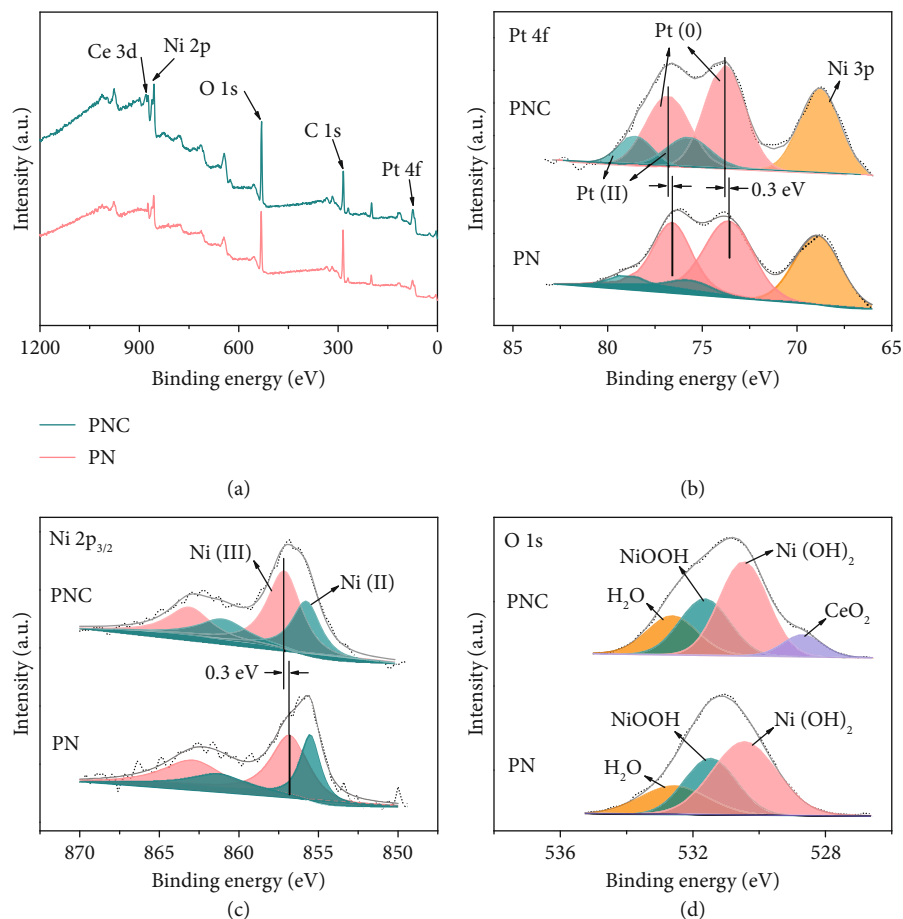
FIGURE 2: XPS spectra. (a) XPS survey spectra of PN and PNC. (b) Pt 4f spectra. (c) Ni 2p$_{3/2}$ region. (d) O 1s region.

while the control Pt/G is granular (Figure 1(c) inset and supplementary Figure S2). This rimous texture and interlinked lamellar morphology would facilitate the penetration of electrolyte inside the electrode and increase the active site exposure area. Contact angle tests indicate superhydrophilic property of PNC (supplementary Figure S3), which can be attributed to the rimous texture and the presence of O−H bond in hydroxide nanosheets. TEM images (Figure 1(c) and supplementary Figure S4) show uniform dispersion of Pt NPs on the hydroxide support. The average size of Pt NPs is 3.1 nm in PNC, smaller than PN (3.4 nm) and Pt/G (13.2 nm). The superhydrophilic surfaces of NC favor the nucleation and growth of Pt, leading to smaller NPs and uniform distribution [32, 33]. The high dispersion of Pt NPs on the mosaic structure of CeO$_2$ and the weak crystallinity of Ni(OH)$_2$ would enrich the interface between metal and oxide/hydroxide. High-resolution TEM (HRTEM) reveals lattice spacings of 0.314 and 0.227 nm (Figure 1(d)), which are separately assigned to the (111) planes of fcc CeO$_2$ and fcc Pt. Energy dispersive spectroscopy (EDS) mapping further confirms the homogenous distribution of Pt, Ni, Ce, and O in PNC (supplementary Figure S5). As detected by EDS and inductively coupled plasma atomic emission spectroscopy (ICP-AES) (supplementary Figure S6), the Pt loadings are 8.8 and 8.2 wt.% in PN and PNC,

respectively. The Pt content could be tuned by adjusting the electrodeposition time in H$_2$PtCl$_6$ solution (supplementary Table S1).

The oxidation states of Pt, Ni(OH)$_2$, and CeO$_2$ were detected by X-ray photoelectron spectroscopy (XPS) spectra (Figure 2). The survey spectra confirm the presence of Pt, Ni, and O in PN and additional Ce in PNC (Figure 2(a)). As shown in Figure 2(b), Pt 4f spectra display two pairs of peaks (4f$_{7/2}$ and 4f$_{5/2}$), corresponding to dominant Pt(0) (75.9%) and surface Pt(II) (24.1%) in PNC. For PN, the atomic ratio of Pt(0) and Pt(II) is 90.7% and 9.3%, respectively. The higher Pt(II) content and 0.3 eV positive shift of Pt(0) peaks in PNC compared to PN suggest partial oxidation of Pt and electronic interaction between Pt and NC [28, 34, 35]. The peak shift also indicates a downshift of the d-band center of Pt in PNC, which could favor hydrogen adsorption on Pt and accelerate the recombination of H$_{ad}$ to form H$_2$ [36–38].

As discerned by Ni 2p XPS spectra (Figure 2(c)), both Ni (II) (855.6 eV) and Ni (III) (857.1 and 856.8 eV) exist in PNC and PN. There is a 0.3 eV positive shift of Ni(III) in PNC, indicating electron transfer from Ni to Ce. The electron-pulling ability of ceria would accelerate the generation of NiOOH active sites for OER. In addition, the coexistence of Ni 3p peak in the Pt 4f region confirms Ni(II) species in Ni(OH)$_2$ [39]. The O 1s spectrum (Figure 2(d)) of PNC
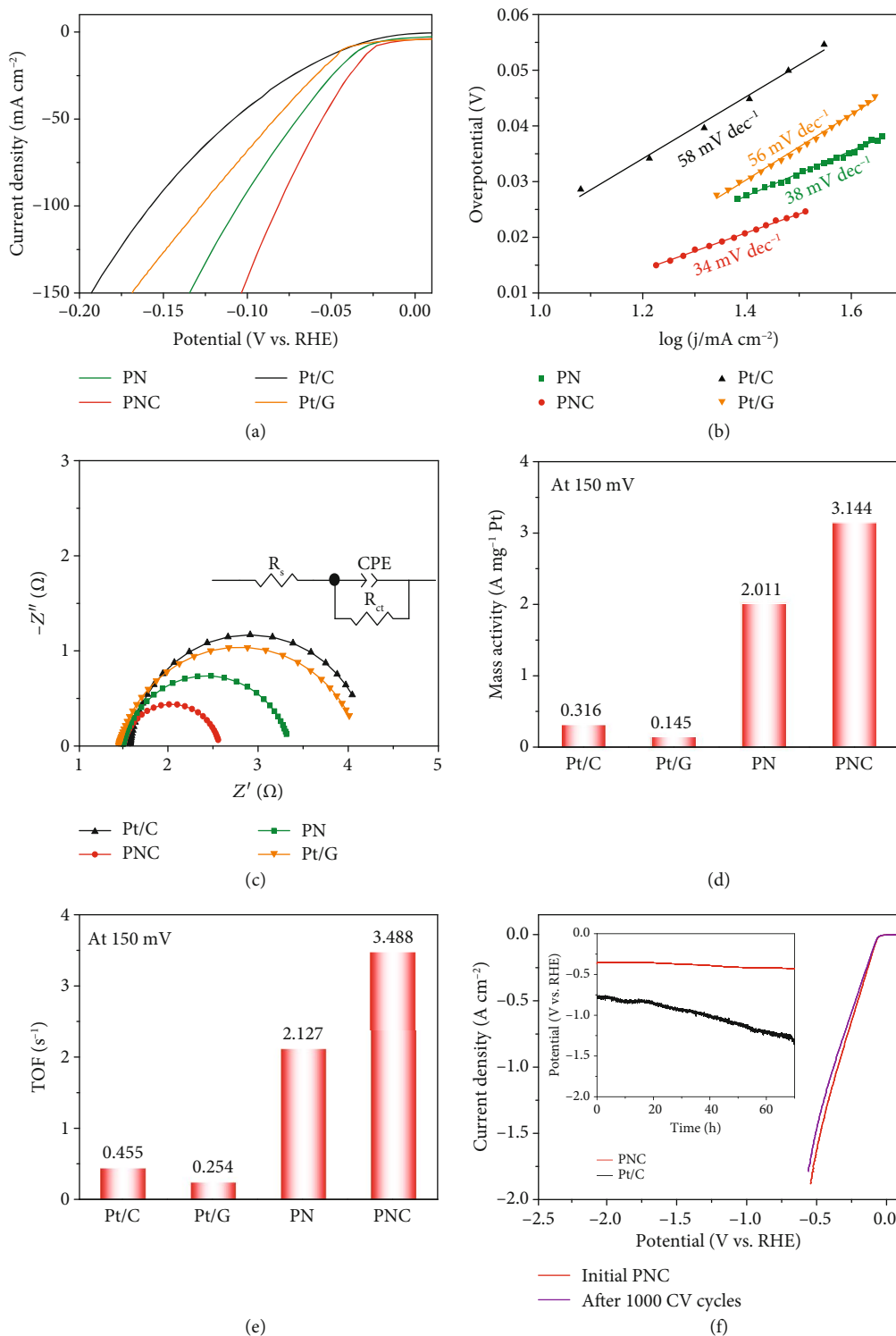
FIGURE 3: HER performance. (a) HER LSV curves and (b) Tafel plots of Pt/C, Pt/G, PN, and PNC in 1.0 M KOH. (c) EIS Nyquist plots. (d) Pt mass activities at the overpotential of 150 mV. (e) Turnover frequency (TOF) deduced from the LSV curves at overpotential of 150 mV. (f) LSV curves of PNC before and after 1000 cycles. The inset shows the chronopotentiometry (*E-t*) curves of PNC and Pt/C at 1000 mA cm^{-2}.

shows deconvoluted peaks at 528.6, 530.5, 531.6, and 532.6 eV assigned to CeO_2, $Ni(OH)_2$, $NiOOH$, and H_2O, respectively [26, 40]. Collecting XPS results suggest strong electron interaction and synergy effect between Pt and Ce-

Ni oxide/hydroxide in PNC, which would favor the formation of more electrocatalytically active species [26, 41].

The electrocatalytic HER performances were investigated by linear sweep voltammetry (LSV). As shown in Figure 3(a),

the onset potential of PNC is near 0 mV and it needs only 76 mV overpotential at $100\,\mathrm{mA\,cm^{-2}}$, significantly outperforming PN (105 mV), Pt/G (124 mV), and 20 wt.% Pt/C (153 mV). At a high applied current density, rapid generation and release of bubbles occur while no catalyst desquamating from the electrode surface is observed for PNC (supplementary Movie S1). The results indicate superior mechanical stability of the electrodeposited hybrid material, which is favorable for industrial application operating under large current density.

Tafel slope is a figure-of-merit to assess HER kinetics of electrocatalysts. In Figure 3(b), the PNC represents a Tafel slope of $38\,\mathrm{mV\,dec^{-1}}$, which is much smaller than PN, Pt/C, and Pt/G (45, 56, and $58\,\mathrm{mV\,dec^{-1}}$) and indicates rapid HER kinetics in PNC (Tafel-Volmer mechanism). The HER process in alkaline condition includes the Volmer adsorption step ($H_2O + e^- \longrightarrow H_{ad} + OH^-$) combined with the Heyrovsky desorption step ($H_{ad} + H_2O + e^- \longrightarrow H_2 + OH^-$) or the Tafel recombination step ($H_{ad} + H_{ad} \longrightarrow H_2$) [42, 43]. In alkaline media, the Volmer step is suggested to determine the HER rate of Pt, due to the sluggish dissociation of water [44, 45]. For the PNC hybrid, the metal (hydro)oxides are efficient to split O−H bond and accelerate the Volmer step, leading to an improvement in HER kinetics. The electrode kinetics of the HER process is further investigated by conducting the EIS experiments, where the equivalent circuit was composed of an electrolyte resistance (R_s) in series with a parallel connection of a constant phase element (CPE) and a charge-transfer resistance (R_{ct}) [46]. From the Nyquist plots (Figure 3(c)) recorded at the potential of −0.026 V vs. RHE, PNC has a smaller R_{ct} compared to Pt/C, Pt/G, and PN. The enhanced charge transfer is attributed to the interfacial electron interaction, plate-like nanostructure with shorter diffusion pathway, and rimous texture that allows facile electrolyte access.

The mass activities were calculated to evaluate the utilization ratio of Pt in the catalysts (Figure 3(d)). At the overpotential of 150 mV, the PNC electrode achieves a remarkable current density of $3.144\,\mathrm{A\,mg^{-1}_{Pt}}$, which is almost 10 and 1.6 times those of the counterpart 20 wt.% Pt/C and PN (0.316 and $2.011\,\mathrm{A\,mg^{-1}_{Pt}}$). The improvement of the mass activity of Pt could be ascribed to the high dispersion and ultrafine particle of Pt. The highest HER activities of PN and PNC are attained when the Pt mass loadings are 8.8 wt.% and 8.2 wt.%, respectively (supplementary Figure S7). Moreover, cyclic voltammetry (CV) curves at different scan rates are measured to obtain the electrochemical double-layer capacitance (C_{dl}) for evaluating the electrochemical active surface areas (ECSAs) (supplementary Figure S8). The current densities are normalized by ECSA or mass of the catalyst to determine specific activity or mass activity at an overpotential of 150 mV. Clearly, PNC delivers overwhelming values as compared to PN, Pt/C, and Pt/G (supplementary Figure S9). The intrinsic catalytic activity can be further evaluated by the turnover frequency (TOF) [47]. Assuming Pt as HER active site, the calculated TOF of PNC is $3.488\,\mathrm{s^{-1}}$ at overpotential of 150 mV, significantly outperforming PN ($2.127\,\mathrm{s^{-1}}$), Pt/G ($0.254\,\mathrm{s^{-1}}$), and Pt/C

($0.455\,\mathrm{s^{-1}}$) (Figure 3(e)). Besides, PNC exhibits superior HER performance as compared with those of previously reported electrocatalysts (supplementary Table S2).

The long-term catalytic durability was investigated by CV sweeping for 1000 cycles, indicating negligible activity loss of the PNC electrode. The overpotential only slightly increases by 21 mV at $1000\,\mathrm{mA\,cm^{-2}}$, surpassing that of Pt/C (116 mV) (Figure 3(f) and supplementary Figure S10). The catalytic stability of PNC was further tested by chronopotentiometry at a large current density of $1000\,\mathrm{mA\,cm^{-2}}$. As shown in Figure 3(f) inset, PNC shows only a very small increase of overpotential after 70 h test, while Pt/C experiences an apparent increase in polarization. Microscopy imaging on cycled electrode reveals that PNC retains its texture and morphology without noticeable particle agglomeration or inhomogeneous elemental distribution, irrespective of a particle size increase of Pt NPs from 3.1 to 5.6 nm (Supplementary Figure S11). Furthermore, the XRD analysis suggests no phase change, while the XPS results show essentially preservation of the oxidation states of Pt and Ce states but an increase in the proportion of Ni (II) species (supplementary Figure S12). The confinement of Pt NPs in hydroxide and the firm adhesion of electrodeposit on graphite could account for the remarkable catalytic and structural stability at large current density.

The OER performances were also assessed by LSV curves (Figure 4(a)). The PNC exhibits a lower overpotential of 186 mV ($100\,\mathrm{mA\,cm^{-2}}$), as compared to PN (279 mV), RuO_2 (321 mV), and Pt/G (1094 mV). The current fluctuation in the LSV curves of RuO_2 results from the formation of large O_2 bubbles. Differently, PNC manifests enhanced and stable OER performance without rigorous fluctuation or large bubble generation at high current density (supplementary Movie S2). Furthermore, the Tafel slope of PNC is $54\,\mathrm{mV\,dec^{-1}}$, lower than that of PN ($63\,\mathrm{mV\,dec^{-1}}$), RuO_2 ($71\,\mathrm{mV\,dec^{-1}}$), and Pt/G ($95\,\mathrm{mV\,dec^{-1}}$) (Figure 4(b)). Remarkably, the OER activity of PNC is among the highest referencing results (supplementary Table S3).

Figure 4(c) shows the EIS data to assess the OER kinetics. At the potential of 1.474 V vs. RHE, a much lower R_{ct} value ($1.4\,\Omega$) was obtained on PNC, in comparison to PN ($3.7\,\Omega$), Pt/G ($18.4\,\Omega$), and RuO_2 ($3.1\,\Omega$). Continuous CV sweeping was tested to investigate the OER durability of PNC (Figure 4(d)). The OER overpotential at $1000\,\mathrm{mA\,cm^{-2}}$ increases only 12 mV after 1000 cycles, revealing insignificant change as compared with RuO_2 (343 mV) (supplementary Figure S13). In addition, the chronopotentiometric response (Figure 4(d) inset) shows unconspicuous decay at $1000\,\mathrm{mA\,cm^{-2}}$ for 70 h, further indicating superior OER catalytic stability of PNC. A combination of SEM, TEM, EDS, and XRD characterizations indicates no apparent change in morphology, composition, and phase but a slight increase of particle size after extended OER electrocatalysis on PNC (supplementary Figures S14 and 15). Of note is that an increased ratio of NiOOH, which has been regarded as the active center of OER [26, 48], can be analyzed by XPS results (supplementary Figure S15d).

Based on the excellent performances of PNC for both the HER and the OER, a symmetric two-electrode cell was
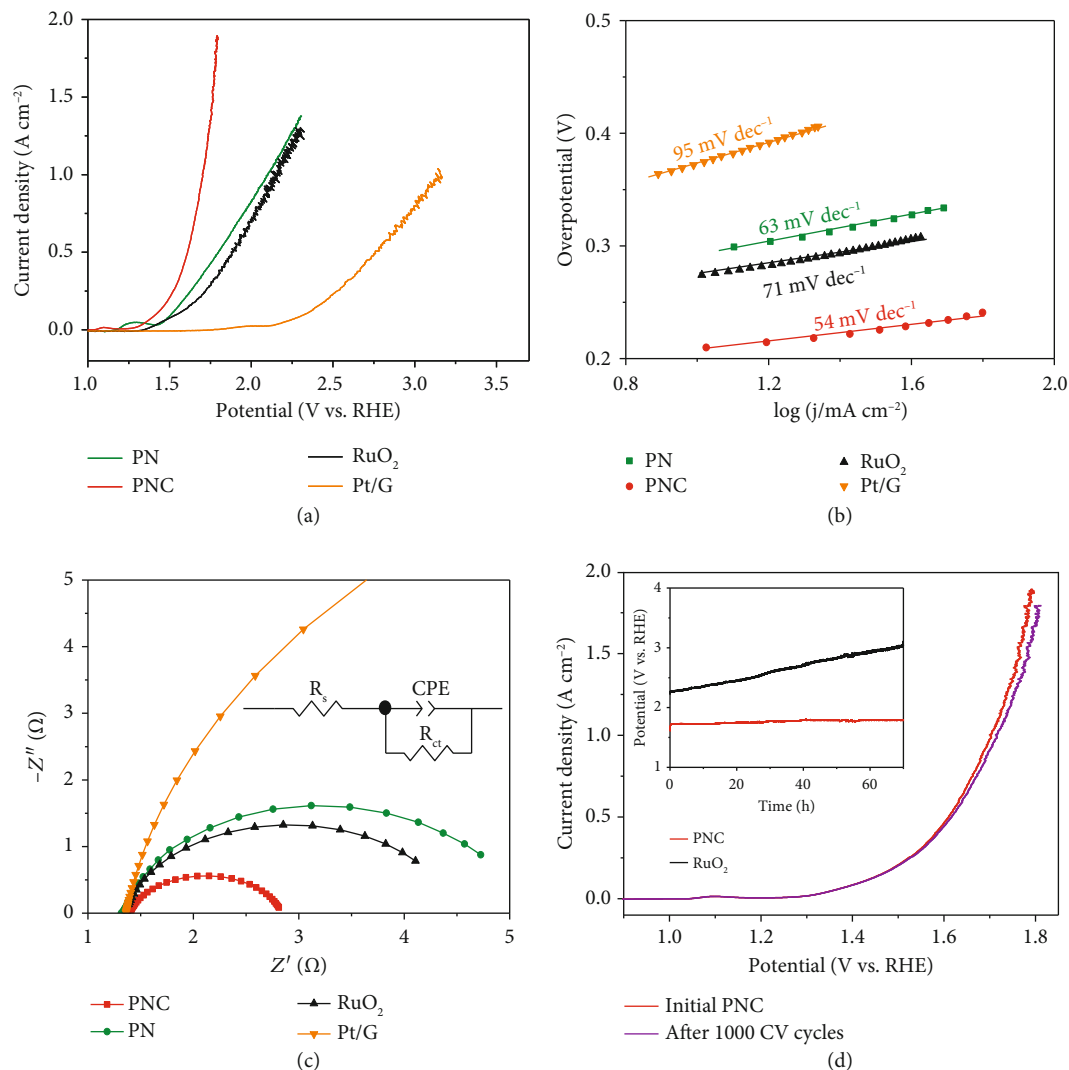
FIGURE 4: OER performance. (a) OER LSV curves and (b) Tafel plots of Pt/G, PN, PNC, and RuO_2 in 1.0 M KOH. (c) EIS Nyquist plots. (d) LSV curves of PNC before and after 1000 OER cycles. The inset shows the chronopotentiometry curves of PNC and RuO_2 at 1000 mA cm^{-2}.

constructed using PNC as a bifunctional electrode for water electrolysis. As shown in Figure 5(a), the cell delivers a current density of 10 mA cm^{-2} at an applied voltage of 1.5 V, 100 mV lower than that of the benchmark Pt/C ‖ RuO_2 couple (1.55 V). The PNC hybrid competes favorably with most electrocatalysts reported previously for overall water splitting (supplementary Table S4). Remarkably, in the extended stability test at a large current density of 1000 mA cm^{-2}, a constant potential of 2.06 V can be well maintained for 85 h with the faintest degradation (Figure 5(b)). A large amount of bubbles release uniformly from the electrode surfaces without any shedding (supplementary Movie S3). Moreover, the volumes of collected H_2 and O_2 match well with the theoretical values as a function of time during electrolysis at 1000 mA cm^{-2} (supplementary Figure S16), indicating nearly 100% faradaic efficiency of PNC ‖ PNC electrolyzer. Excitingly, the PNC-based device can be actuated by a 1.5 V battery for vigorous, stable generation, and release of gas

(supplementary Figure S17 and Movie S3), again confirming the high efficiency of PNC to electrolyze water.

Figure 5(c) schematically shows the reaction mechanism of the electrolyzer. We propose that metal hydroxide in PNC promotes the rupture of O−H in water and the generation of adsorbed H atoms (H_{ads}), which adsorb on the Pt surface to recombine into hydrogen molecule. Meanwhile, the OH$^-$ ions are transformed into O_2 on the anode with different metal centers [22, 26, 49]. To gain further insight into the water dissociation process, we performed preliminary DFT calculations on the configuration and evolution of PNC hybrid and dissociation energy of H_2O on the interface (Figure 5(d) and supplementary Movie S4). The water is adsorbed at the interface of $Ni(OH)_2$ and CeO_2, where O is connected with the Ni atom in $Ni(OH)_2$ and H forms a weak hydrogen bond interaction with O in CeO_2. These interactions jointly promote the activation of water, resulting in the fracture of O−H bond in water and the formation of the final structure in Figure 5(d). The
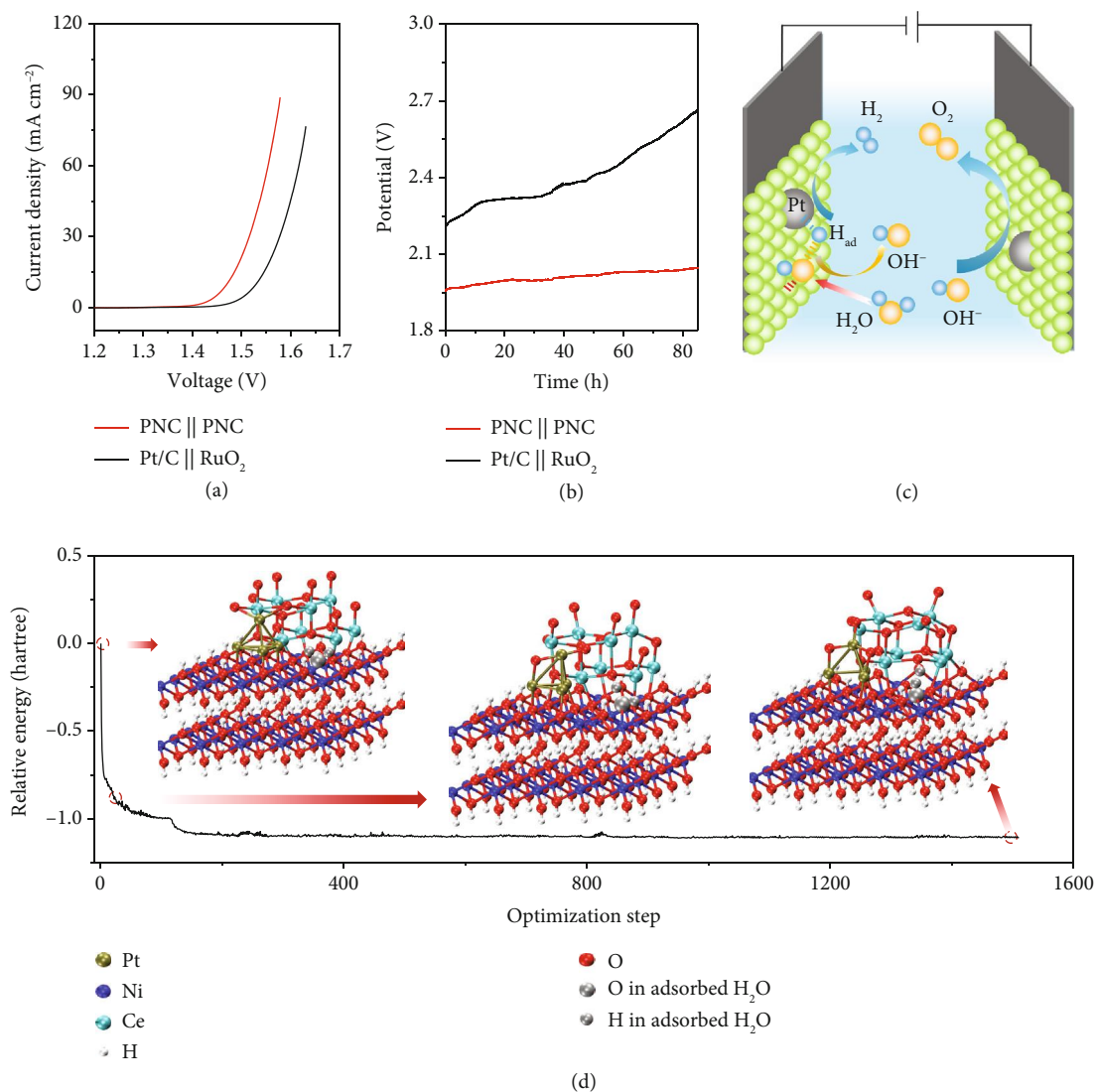
FIGURE 5: Water splitting performance. (a) LSV curves of the PNC || PNC and Pt/C || RuO$_2$ electrolyzers in 1.0 M KOH. (b) Chronopotentiometry curves of PNC || PNC and Pt/C || RuO$_2$ electrolyzers at 1000 mA cm^{-2}. (c) Illustration of the PNC as a bifunctional electrode for overall water electrolysis. (d) DFT calculated the relative energy diagram of the water dissociation process for PNC. The inset shows the structural diagram of PNC at different water decomposition states.

process is exothermic (about −2.74 eV), indicating that water dissociation can proceed spontaneously at this interface. Accordingly, the superior performance of PNC can be attributed to the synergistic effect among Pt, Ni(OH)$_2$, and CeO$_2$ in the hybrid, together with the beneficial texture, microstructure, and wettability.

3. Conclusion

In summary, we report the electrodeposition of Pt-Ni(OH)$_2$-CeO$_2$ hybrid on graphite and its application for efficient electrocatalysis of water splitting. In 1.0 M KOH, the PNC electrode needs only overpotentials of 76 and 186 mV to afford 100 mA cm^{-2} current density for HER and OER, respectively. The turn over frequency and Pt-based mass activity towards HER are significantly improved on PNC than the benchmark Pt/C. Remarkably, when PNC electrode is directly utilized as

the anode and cathode, the assembled symmetric water electrolyzer well works at a low applied cell voltage of 1.45 V. Additionally, respectable stability of PNC is attained at 1000 mA cm^{-2}. The superior activity is due to high dispersion of Pt NPs and electronic interaction among Pt, Ni(OH)$_2$, and CeO$_2$ while the durability is ascribed to strong deposit/graphite adherence, electrode hydrophilicity, and facilitated release of gas bubbles. The results indicate that Pt-decorated hydroxide/oxide electrodeposited on graphite is a promising electrocatalyst for overall water electrolysis.

4. Materials and Methods

4.1. Material Synthesis.
To prepare the PNC hybrid, cathodic galvanostatic electrodeposition was applied and performed using a two-electrode system in a 50 ml electrolytic bath at 25°C. The working and counter electrode are two graphite

plates (1×2 cm) [26]. The graphite plate was first preprocessed by applying an anodic current of $20 \, \text{mA} \, \text{cm}^{-2}$ for 300 s to realize NO_3^- intercalation in the interlamination. Then, a cathodic current of $-20 \, \text{mA} \, \text{cm}^{-2}$ was applied for 300 s in a nitrate solution containing 0.09 M $Ni(NO_3)_2$ and 0.01 M $Ce(NO_3)_3$. After that, cathodic depositions at $-20 \, \text{mA} \, \text{cm}^{-2}$ were performed for different time (50, 100, 150, and 200 s) in 0.02 M H_2PtCl_6 solution. For comparison, PN was obtained from electrodeposition in 0.1 M $Ni(NO_3)_2$ and 0.02 M H_2PtCl_6 using a similar process, while Pt/G was prepared in 0.02 M H_2PtCl_6 at $20 \, \text{mA} \, \text{cm}^{-2}$ for 300 s.

4.2. Material Characterizations. A JEOL JSM-7500F microscope was used to obtain SEM images. TEM and HRTEM were carried out on a FEI Talos F200X G2 system equipped with EDS. A Rigaku MiniFlex 600 diffractometer was used to measure the XRD patterns. XPS data were collected with a Kratos Axis Ultra DLD spectrometer. Elemental analysis was obtained on ICP-AES (PerkinElmer Optima 83000).

4.3. Electrochemical Measurements. All electrochemical tests were tested by a three-electrode system on AMETEK Parstat 4000 electrochemical workstation in 1.0 M KOH. The electrodeposited electrodes, Hg/HgO, and graphite rod were employed as the working, reference, and counter electrode, respectively. To study the HER performance, LSV curves were tested at $10 \, \text{mV} \, \text{s}^{-1}$ from -0.8 to -1.6 V vs. Hg/HgO. The OER activity was tested from 0 to 2.0 V vs. Hg/HgO. To test EIS, the frequency range is set from 100 kHz to 0.01 Hz. Water electrolysis was detected in a two-electrode system, and LSV curves were measured from 1.0 to 2.0 V at $10 \, \text{mV} \, \text{s}^{-1}$. Potentials were reported versus reversible hydrogen electrode (RHE) unless noted, in line with the equation $E \, (\text{RHE}) = 0.924 \, \text{V} + E \, (\text{Hg/HgO})$. All LSV curves have been iR corrected unless otherwise specified.

The C_{dl} values were determined from the double layer region (without faradaic processes) in the CV curves recorded at different scan rates. The ECSA of the prepared catalysts was calculated according to

$$\text{ECSA} = \frac{C_{dl}}{C_s}, \tag{5}$$

where C_{dl} is the double-layer capacitance and C_s is the specific capacitance ($0.040 \, \text{mF} \, \text{cm}^{-2}$) [50].

The TOF was determined by the following equation [51, 52]:

$$\text{TOF} = \frac{J \times A}{2 \times F \times m}, \tag{6}$$

where J is the current density at a given overpotential (150 mV), F is the Faraday constant ($96{,}485 \, \text{C} \, \text{mol}^{-1}$), A is the electrode surface area ($1 \, \text{cm}^2$), and m is the number of moles of active species on the electrode. The Pt content in PN and PNC was quantified by ICP-AES. In TOF calculation, Pt atoms are counted as the active sites in PN and PNC.

4.4. DFT Calculation. Density function theory calculation was performed by using the CP2K package [53]. PBE func-

tional [54] with Grimme D3 correction [55] was used to describe the system. Unrestricted Kohn-Sham DFT has been used as the electronic structure method in the framework of the Gaussian and plane wave method [56, 57]. The Goedecker-Teter-Hutter (GTH) pseudopotentials [58, 59] and DZVPMOLOPT-GTH basis sets [56] were utilized to describe the molecules. A plane-wave energy cut-off of 500 Ry has been employed.

Conflicts of Interest

The authors declare no conflict of interest.

Authors' Contributions

F. Y. Cheng and Z. H. Yan supervised the research. H. H. Liu carried out the experiments, measured and analyzed the data, and drafted the manuscript. X. Chen, J. H. Li, and L. Zhang participated in electrochemical measurements. J. H. Li, F. M. Liu, and G. L. Fan assisted material characterization and DFT calculation. All the authors participated in the discussion of results and manuscript.

Acknowledgments

Supplementary Materials

Figure S1: powder XRD patterns of $Ni(OH)_2$ and NC scratched down from the Ti mesh. Figure S2: SEM images of Pt/G (a, b), PN (c, d), and PNC (e, f) at low (a, c, e) and high (b, d, f) magnification. Figure S3: contact angles measured on graphite substrate (a) before and (b–d) after the electrodeposition of Pt (b), PN (c), and PNC (d). Figure S4: (a, b) TEM images and particle size distribution of PN. (c, d) TEM images and particle size distribution of Pt/G. Figure S5: elemental mapping images of PNC. Figure S6: EDS spectra of (a) Pt, (b) PN, and (c) PNC. Figure S7: HER polarization curves of (a) PN and (b) PNC hybrid with different Pt loadings. Figure S8: CV curves of (a) Pt/C, (b) electrodeposited Pt, (c) PN, and (d) PNC. (e) The corresponding linear fitting of the current density versus scan rates. (f) Comparison of ECSA. Figure S9: (a) specific and mass activities derived from the HER polarization curves at 150 mV. Figure S10: polarization curves of 20 wt.% Pt/C before and after 1000 HER cycles. Figure S11: (a) SEM, (b) TEM, (c) HRTEM, and (d) elemental mapping images of PNC after 70 h of HER stability test at $1000 \, \text{mA} \, \text{cm}^{-2}$. Insets (a) and (b) show high-magnification SEM image and size distribution of Pt nanoparticles, respectively. Figure S12: (a) XRD pattern of PNC after HER stability test for 70 h at $1000 \, \text{mA} \, \text{cm}^{-2}$. High-resolution XPS spectra of (b) Pt 4f, (c) Ni 2p3/2, and (d) O 1s of PNC after stability test. Figure

S13: polarization curves of RuO_2 before and after 1000 OER cycles. Figure S14: (a) SEM, (b) TEM, (c) HRTEM, and (d) elemental mapping images of PNC after 70 h of OER stability test at $1000 \, mA \, cm^{-2}$. Insets (a) and (b) show high-magnification SEM image and size distribution of Pt nanoparticles, respectively. Figure S15: (a) XRD patterns of PNC after OER stability test. High-resolution XPS spectra of (b) Pt 4f, (c) Ni 2p3/2, and (d) O 1s regions of PNC after stability test. Figure S16: generated and theoretical volumes of H_2 and O_2 over time at a constant current density of $1000 \, mA \, cm^{-2}$ in PNC || PNC electrolyzer. Figure S17: digital photographs of the PNC || PNC electrolyzer powered by a 1.5 V battery. Table S1: Pt contents in PN and PNC with different electrodeposition time in the H_2PtCl_6 precursor solutions. Table S2: the comparison of HER performances of PNC with other electrocatalysts. Table S3: the comparison of OER performances of PNC with other electrocatalysts. Table S4: comparison of water splitting performance of PNC electrocatalyst with other bifunctional electrocatalysts reported before. Movie S1: the formation and release of bubbles on the PNC electrode surface for HER at different current densities. Movie S2: the formation and release of bubbles on the PNC electrode surface for OER at different current densities. Movie S3: the process of water splitting at different densities and the gas generation and release on electrode surface when the PNC || PNC electrolyzer is powered by a 1.5 V battery. Movie S4: the movie of DFT calculated the water dissociation process on the PNC interface. *(Supplementary Materials)*

References

[1] R. F. Service, "The hydrogen backlash," *Science*, vol. 305, no. 5686, pp. 958–961, 2004.

[2] K. S. Joya, Y. F. Joya, K. Ocakoglu, and R. van de Krol, "Water-splitting catalysis and solar fuel devices: artificial leaves on the move," *Angewandte Chemie International Edition*, vol. 52, no. 40, pp. 10426–10437, 2013.

[3] C. C. L. McCrory, S. Jung, I. M. Ferrer, S. M. Chatman, J. C. Peters, and T. F. Jaramillo, "Benchmarking hydrogen evolving reaction and oxygen evolving reaction electrocatalysts for solar water splitting devices," *Journal of the American Chemical Society*, vol. 137, no. 13, pp. 4347–4357, 2015.

[4] L. Wu, L. Yu, X. Xiao et al., "Recent advances in self-supported layered double hydroxides for oxygen evolution reaction," *Research*, vol. 2020, article 3976278, 17 pages, 2020.

[5] N. Jiang, B. You, M. Sheng, and Y. Sun, "Electrodeposited cobalt-phosphorous-derived films as competent bifunctional catalysts for overall water splitting," *Angewandte Chemie International Edition*, vol. 54, no. 21, pp. 6251–6254, 2015.

[6] Q. Gao, R. Wu, Y. Liu et al., "Synthesis of PdS_x-mediated polydymite heteronanorods and their long-range activation for enhanced water electroreduction," *Research*, vol. 2019, article 8078549, 11 pages, 2019.

[7] H. Sun, X. Xu, Z. Yan et al., "Porous multishelled Ni_2P hollow microspheres as an active electrocatalyst for hydrogen and oxygen evolution," *Chemistry of Materials*, vol. 29, no. 19, pp. 8539–8547, 2017.

[8] Y. Lee, J. Suntivich, K. J. May, E. E. Perry, and Y. Shao-Horn, "Synthesis and activities of rutile IrO_2 and RuO_2 nanoparticles for oxygen evolution in acid and alkaline solutions," *Journal of Physical Chemistry Letters*, vol. 3, no. 3, pp. 399–404, 2012.

[9] X. Zhao, J. Meng, Z. Yan, F. Cheng, and J. Chen, "Nanostructured $NiMoO_4$ as active electrocatalyst for oxygen evolution," *Chinese Chemical Letters*, vol. 30, no. 2, pp. 319–323, 2019.

[10] H. Zhu, J. Zhang, R. Yanzhang et al., "When cubic cobalt sulfide meets layered molybdenum disulfide: a core–shell system toward synergetic electrocatalytic water splitting," *Advanced Materials*, vol. 27, no. 32, pp. 4752–4759, 2015.

[11] H. Shi, Y. T. Zhou, R. Q. Yao et al., "Intermetallic Cu_5Zr clusters anchored on hierarchical nanoporous copper as efficient catalysts for hydrogen evolution reaction," *Research*, vol. 2020, article 2987234, 12 pages, 2020.

[12] H. Sun, X. Xu, Z. Yan et al., "Superhydrophilic amorphous Co–B–P nanosheet electrocatalysts with Pt-like activity and durability for the hydrogen evolution reaction," *Journal of Materials Chemistry A*, vol. 6, no. 44, pp. 22062–22069, 2018.

[13] R. Subbaraman, D. Tripkovic, K. C. Chang et al., "Trends in activity for the water electrolyser reactions on 3d M(Ni,Co,Fe,Mn) hydr(oxy)oxide catalysts," *Nature Materials*, vol. 11, no. 6, pp. 550–557, 2012.

[14] X. Zheng, B. Zhang, P. de Luna et al., "Theory-driven design of high-valence metal sites for water oxidation confirmed using in situ soft X-ray absorption," *Nature Chemistry*, vol. 10, no. 2, pp. 149–154, 2018.

[15] F. Dionigi and P. Strasser, "NiFe-based (oxy)hydroxide catalysts for oxygen evolution reaction in non-acidic electrolytes," *Advanced Energy Materials*, vol. 6, no. 23, article 1600621, 2016.

[16] B. E. Conway and G. Jerkiewicz, "Nature of electrosorbed H and its relation to metal dependence of catalysis in cathodic H_2 evolution," *Solid State Ionics*, vol. 150, no. 1-2, pp. 93–103, 2002.

[17] B. Ruqia and S. I. Choi, "Pt and Pt–Ni(OH)$_2$ Electrodes for the hydrogen evolution reaction in alkaline electrolytes and their nanoscaled electrocatalysts," *ChemSusChem*, vol. 11, no. 16, pp. 2643–2653, 2018.

[18] D. Strmcnik, P. P. Lopes, B. Genorio, V. R. Stamenkovic, and N. M. Markovic, "Design principles for hydrogen evolution reaction catalyst materials," *Nano Energy*, vol. 29, pp. 29–36, 2016.

[19] G. Wang, J. Parrondo, C. He, Y. Li, and V. Ramani, "Pt/C/Ni(OH)$_2$ Bi-Functional electrocatalyst for enhanced hydrogen evolution reaction activity under alkaline conditions," *Journal of the Electrochemical Society*, vol. 164, no. 13, pp. F1307–F1315, 2017.

[20] L. Wang, Y. Zhu, Z. Zeng et al., "Platinum−nickel hydroxide nanocomposites for electrocatalytic reduction of water," *Nano Energy*, vol. 31, pp. 456–461, 2017.

[21] H. Yin, S. Zhao, K. Zhao et al., "Ultrathin platinum nanowires grown on single-layered nickel hydroxide with high hydrogen evolution activity," *Nature Communications*, vol. 6, no. 1, article 6430, 2015.

[22] R. Subbaraman, D. Tripkovic, D. Strmcnik et al., "Enhancing hydrogen evolution activity in water splitting by tailoring Li$^+$−Ni(OH)$_2$−Pt interfaces," *Science*, vol. 334, no. 6060, pp. 1256–1260, 2011.

[23] Y. Wang, L. Chen, X. Yu, Y. Wang, and G. Zheng, "Superb alkaline hydrogen evolution and simultaneous electricity generation by Pt-decorated Ni_3N nanosheets," *Advanced Energy Materials*, vol. 7, no. 2, article 1601390, 2017.

[24] C. Chen, Y. Kang, Z. Huo et al., "Highly crystalline multimetal-lic nanoframes with three-dimensional electrocatalytic surfaces," *Science*, vol. 343, no. 6177, pp. 1339–1343, 2014.

[25] Y. Zhu, W. Zhou, Y. Zhong et al., "A perovskite nanorod as bifunctional electrocatalyst for overall water splitting," *Advanced Energy Materials*, vol. 7, no. 8, article 1602122, 2017.

[26] Z. Yan, H. Sun, X. Chen et al., "Anion insertion enhanced electrodeposition of robust metal hydroxide/oxide electrodes for oxygen evolution," *Nature Communications*, vol. 9, no. 1, article 2373, 2018.

[27] G. Fan, H. Sun, F. Cheng, and J. Chen, "Progress in DFT study on 3d transition metal oxide/hydroxide electrocatalyst for oxygen evolution," *Scientia Sinica Chimica*, vol. 49, no. 5, pp. 741–751, 2019.

[28] A. Bruix, J. A. Rodriguez, P. J. Ramírez et al., "A new type of strong metal-support interaction and the production of H_2 through the transformation of water on $Pt/CeO_2(111)$ and $Pt/CeO_x/TiO_2(110)$ catalysts," *Journal of the American Chemical Society*, vol. 134, no. 21, pp. 8968–8974, 2012.

[29] J. Park, H. Wang, M. Vara, and Y. Xia, "Platinum cubic nanoframes with enhanced catalytic activity and durability toward oxygen reduction," *ChemSusChem*, vol. 9, no. 19, pp. 2855–2861, 2016.

[30] E. Jung, H. Y. Park, A. Cho, J. H. Jang, H. S. Park, and T. Yu, "Aqueous-phase synthesis of metal hydroxide nanoplates and platinum/nickel hydroxide hybrid nanostructures and their enhanced electrocatalytic properties," *Applied Catalysis B: Environmental*, vol. 225, pp. 238–242, 2018.

[31] R. Kavian, S. I. Choi, J. Park et al., "Pt–Ni octahedral nanocrystals as a class of highly active electrocatalysts toward the hydrogen evolution reaction in an alkaline electrolyte," *Journal of Materials Chemistry A*, vol. 4, no. 32, pp. 12392–12397, 2016.

[32] Y. Liu, C. M. Hangarter, D. Garcia, and T. P. Moffat, "Self-terminating electrodeposition of ultrathin Pt films on Ni: an active, low-cost electrode for H_2 production," *Surface Science*, vol. 631, pp. 141–154, 2015.

[33] Y. Zhou, J. M. Perket, and J. Zhou, "Growth of Pt nanoparticles on reducible $CeO_2(111)$ thin films: effect of nanostructures and redox properties of ceria," *Journal of Physical Chemistry C*, vol. 114, no. 27, pp. 11853–11860, 2010.

[34] H. Feng, Z. Xu, L. Ren et al., "Activating titania for efficient electrocatalysis by vacancy engineering," *ACS Catalysis*, vol. 8, no. 5, pp. 4288–4293, 2018.

[35] X. Zheng, P. Cui, Y. Qian et al., "Multifunctional active-center-transferable platinum/lithium cobalt oxide heterostructured electrocatalysts towards superior water splitting," *Angewandte Chemie International Edition*, vol. 59, no. 34, pp. 14533–14540, 2020.

[36] M. Lao, K. Rui, G. Zhao et al., "Platinum/nickel bicarbonate heterostructures towards accelerated hydrogen evolution under alkaline conditions," *Angewandte Chemie International Edition*, vol. 58, no. 16, pp. 5432–5437, 2019.

[37] X. Cheng, Y. Li, L. Zheng et al., "Highly active, stable oxidized platinum clusters as electrocatalysts for the hydrogen evolution reaction," *Energy & Environmental Science*, vol. 10, no. 11, pp. 2450–2458, 2017.

[38] V. R. Stamenkovic, B. S. Mun, M. Arenz et al., "Trends in electrocatalysis on extended and nanoscale Pt-bimetallic alloy surfaces," *Nature Materials*, vol. 6, no. 3, pp. 241–247, 2007.

[39] J. Ji, L. L. Zhang, H. Ji et al., "Nanoporous $Ni(OH)_2$ thin film on 3D ultrathin-graphite foam for asymmetric supercapacitor," *ACS Nano*, vol. 7, no. 7, pp. 6237–6243, 2013.

[40] A. N. Mansour and C. A. Melendres, "Characterization of α-$Ni(OH)_2$ by XPS," *Surface Science Spectra*, vol. 3, no. 3, pp. 255–262, 1994.

[41] T. Tang, W. J. Jiang, S. Niu et al., "Electronic and morphological dual modulation of cobalt carbonate hydroxides by Mn doping toward highly efficient and stable bifunctional electrocatalysts for overall water splitting," *Journal of the American Chemical Society*, vol. 139, no. 24, pp. 8320–8328, 2017.

[42] Y. Liu, Q. Li, R. Si et al., "Coupling sub-nanometric copper clusters with quasi-amorphous cobalt sulfide yields efficient and robust electrocatalysts for water splitting reaction," *Advanced Materials*, vol. 29, no. 13, article 1606200, 2017.

[43] X. Ma, W. Zhang, Y. Deng, C. Zhong, W. Hu, and X. Han, "Phase and composition controlled synthesis of cobalt sulfide hollow nanospheres for electrocatalytic water splitting," *Nanoscale*, vol. 10, no. 10, pp. 4816–4824, 2018.

[44] J. O.'. M. Bockris, "The origin of ideas on a hydrogen economy and its solution to the decay of the environment," *International Journal of Hydrogen Energy*, vol. 27, no. 7-8, pp. 731–740, 2002.

[45] J. Durst, A. Siebel, C. Simon, F. Hasché, J. Herranz, and H. A. Gasteiger, "New insights into the electrochemical hydrogen oxidation and evolution reaction mechanism," *Energy and Environmental Science*, vol. 7, no. 7, pp. 2255–2260, 2014.

[46] X. Long, G. Li, Z. Wang et al., "Metallic iron–nickel sulfide ultrathin nanosheets as a highly active electrocatalyst for hydrogen evolution reaction in acidic media," *Journal of the American Chemical Society*, vol. 137, no. 37, pp. 11900–11903, 2015.

[47] X. Zou and Y. Zhang, "Noble metal-free hydrogen evolution catalysts for water splitting," *Chemical Society Reviews*, vol. 44, no. 15, pp. 5148–5180, 2015.

[48] S. Lee, K. Banjac, M. Lingenfelder, and X. Hu, "Oxygen isotope labeling experiments reveal different reaction sites for the oxygen evolution reaction on nickel and nickel iron oxides," *Angewandte Chemie International Edition*, vol. 58, no. 30, pp. 10295–10299, 2019.

[49] P. A. Thiel and T. E. Madey, "The interaction of water with solid surfaces: fundamental aspects," *Surface Science Reports*, vol. 46, no. 1-8, pp. 1–308, 2002.

[50] S. Niu, W. J. Jiang, T. Tang, L. P. Yuan, H. Luo, and J. S. Hu, "Autogenous growth of hierarchical $NiFe(OH)_x/FeS$ nanosheet-on-microsheet arrays for synergistically enhanced high-output water oxidation," *Advanced Functional Materials*, vol. 29, no. 36, p. 1902180, 2019.

[51] X. Lu and C. Zhao, "Electrodeposition of hierarchically structured three-dimensional nickel–iron electrodes for efficient oxygen evolution at high current densities," *Nature Communications*, vol. 6, no. 1, article 6616, 2015.

[52] L. Zhang, Z. Yan, X. Chen et al., "Facile synthesis of amorphous MoS_x-Fe anchored on Zr-MOFs towards efficient and stable electrocatalytic hydrogen evolution," *Chemical Communications*, vol. 56, no. 18, pp. 2763–2766, 2020.

[53] J. Hutter, M. Iannuzzi, F. Schiffmann, and J. VandeVondele, "Cp2k: atomistic simulations of condensed matter systems," *Wiley Interdisciplinary Reviews: Computational Molecular Science*, vol. 4, no. 1, pp. 15–25, 2014.

[54] J. P. Perdew, K. Burke, and M. Ernzerhof, "Generalized gradient approximation made simple," *Physical Review Letters*, vol. 77, no. 18, pp. 3865–3868, 1996.

[55] S. Grimme, "Semiempirical gga-type density functional constructed with a long-range dispersion correction," *Journal of Computational Chemistry*, vol. 27, no. 15, pp. 1787–1799, 2006.

[56] J. VandeVondele and J. Hutter, "Gaussian basis sets for accurate calculations on molecular systems in gas and condensed phases," *The Journal of Chemical Physics*, vol. 127, no. 11, article 114105, 2007.

[57] J. VandeVondele, M. Krack, F. Mohamed, M. Parrinello, T. Chassaing, and J. Hutter, "Quickstep: fast and accurate density functional calculations using a mixed gaussian and plane waves approach," *Computer Physics Communications*, vol. 167, no. 2, pp. 103–128, 2005.

[58] S. Goedecker, M. Teter, and J. Hutter, "Separable dual-space Gaussian pseudopotentials," *Physical Review B*, vol. 54, no. 3, pp. 1703–1710, 1996.

[59] C. Hartwigsen, S. Goedecker, and J. Hutter, "Relativistic separable dual-space Gaussian pseudopotentials from H to Rn," *Physical Review B*, vol. 58, no. 7, pp. 3641–3662, 1998.